

PAH emission from star-forming galaxies in *JWST* mid-infrared imaging of the lensing cluster SMACS J0723.3–7327

DANIAL LANGEROODI¹ AND JENS HJORTH¹

¹*DARK, Niels Bohr Institute, University of Copenhagen, Jagtvej 128, 2200 Copenhagen, Denmark*

Submitted to ApJ Letters

ABSTRACT

The mid-infrared spectra of star-forming galaxies (SFGs) are characterized by characteristic broad PAH emission features at 3–20 μm . As these features are redshifted, they are predicted to dominate the flux at specific mid-infrared wavelengths, leading to substantial redshift-dependent color variations in broad-band photometry. The advent of *JWST* for the first time allows the study of this effect for normal SFGs. Based on spectral energy distribution templates, we here present tracks in mid-infrared (4.4, 7.7, 10, 15, and 18 μm) color-color diagrams describing the redshift dependence of SFG colors. In addition, we present simulated color-color diagrams by populating these tracks using the cosmic star-formation history and the star-formation rate function. Depending on redshift, we find that SFGs stand out in the color-color diagrams by several magnitudes. We provide the first observational demonstration of this effect for galaxies detected in the *JWST* Early Release Observations of the field towards the lensing cluster SMACS J0723.3–7327. While the distribution of detected galaxies is consistent with the simulations, the numbers are substantially boosted by lensing effects. The PAH emitter with the highest spectroscopic redshift, detected in all bands, is a multiply-imaged galaxy at $z = 1.45$. There is also a substantial number of cluster members, which do not exhibit PAH emission, except for one SFG at $z = 0.38$. Future wider-field observations will further populate mid-infrared color-color diagrams and provide insight into the evolution of typical SFGs.

Keywords: Polycyclic aromatic hydrocarbons (1280) - Galaxy photometry (611) - Galaxy colors (586) - *JWST* (2291)

1. INTRODUCTION

When excited by radiation in star-forming (SF) regions, polycyclic aromatic hydrocarbons (PAHs) give rise to characteristic emission features in the mid-infrared range, notably at 3.3, 6.2, 7.7, 8.6, and 11.3 μm . This emission may account for as much as 10–20% of the infrared luminosity in starburst galaxies, and the 7.7 μm feature alone may account for 50 % of the total PAH luminosity (Draine & Li 2007; Smith et al. 2007; Wu et al. 2010; Shipley et al. 2013). As such, PAH luminosity is an excellent star-formation rate (SFR) indicator for galaxies in the nearby universe (e.g., Förster Schreiber et al. 2004; Treyer et al. 2010; Shipley et al. 2016; Xie & Ho 2019).

At low redshifts ($z \lesssim 0.3$), PAH emission based mid-infrared color selections of star-forming galaxies (SFGs)

and active galactic nuclei (AGNs) have been carried out using photometry from the *Infrared Space Observatory* (*ISO*) or the *Spitzer Space Telescope* (Laurent et al. 2000; Veilleux et al. 2009). Due to the limited sensitivity of *Spitzer*, observations of PAH features at higher redshifts ($z \sim 0.3 - 2.8$) have been limited to bright (ultra) luminous infrared galaxies (LIRGs) and AGNs (Pope et al. 2008; Kirkpatrick et al. 2015).

The Mid Infrared Instrument (MIRI) aboard *JWST* offers an unprecedented opportunity to study the properties of much fainter galaxies at mid-infrared wavelengths. Gravitational lensing may provide an additional boost in sensitivity (Mason et al. 2015). Kirkpatrick et al. (2017) (see also Inami et al. 2018) predicted the properties of galaxies in MIRI bands, with emphasis on high-redshift ($z \sim 1 - 2$) luminous galaxies and the possible contribution of AGN to their colors (see Pope et al. 2008, for a similar study, focused on *Spitzer*/IRAC colors at $z > 1$). The combination of depth and pho-

tometric coverage provided by *JWST* broad-band imaging suggest that normal lower-luminosity star-forming galaxies will be detected frequently over a wide redshift range ($z \sim 0-2$).

Depending on redshift, PAH features will substantially affect the flux of star-forming galaxies in broad MIRI bands. For instance, the $7.7 \mu\text{m}$ PAH emission feature is expected to contribute strongly to the flux observed in the MIRI F770W, F1000W, F1500W, or F1800W bands at redshifts 0, 0.3, 1, and 1.3, respectively. Tracing this feature at higher redshifts becomes challenging, as the longer wavelength MIRI bands become less sensitive. Bluer filters (NIRCam F444W or MIRI F560W, F770W) may provide a short-wavelength baseline band which is largely unaffected by PAH emission (although these filters can be sensitive to $3.3 \mu\text{m}$ emission, depending on redshift; see, e.g., [Sajina et al. 2009](#); [Inami et al. 2018](#)). This unique combination of redder PAH-sensitive and bluer PAH-unaffected filters can be used to identify normal SFGs with PAH-dominated mid-infrared spectra, based on their location in color-color diagrams.

In this Letter we explore the redshift evolution of the mid-infrared properties of normal SFGs as seen in the broad-band photometry of *JWST*. We generate simulated color-color diagrams (in the F444W, F770W, F1000W, F1500W, and F1800W filters) of field SFGs and compare them with those constructed from our analysis of the *JWST* Early Release Observations ([Pontoppidan et al. 2022](#)) towards the SMACS J0723.3–7327 cluster of galaxies (SMACS J0723 for short) at $z = 0.4$, where lensing may enhance the detection of fainter, higher-redshift SFGs. This provides the first observational demonstration of how normal SFGs populate *JWST* mid-infrared color-color diagrams.

2. TRACKS IN COLOR-COLOR DIAGRAMS

We model the redshift-dependent tracks in the NIRCam and MIRI mid-infrared color-color diagrams using the empirically-calibrated galaxy spectral energy distribution (SED) templates of [Dale & Helou \(2002\)](#) and [Kirkpatrick et al. \(2012\)](#). [Dale & Helou \(2002\)](#) created semi-empirical SED templates from 0.36 to $1100 \mu\text{m}$, constrained in the $3-100 \mu\text{m}$ range against IRAS, ISOCAM, and ISOPHOT observations of 69 nearby normal SFGs; in the $52-170 \mu\text{m}$ range against ISOLWS data of 228 galaxies; and at $850 \mu\text{m}$ against SCUBA observations of 110 galaxies. [Dale & Helou \(2002\)](#) parameterized their semi-empirical spectra based on the far-infrared flux density ratio $f_v(60\mu\text{m})/f_v(100\mu\text{m})$ (ranging from 0.3 to 1.6; providing an indicator of dust grain temperature), generating templates that describe the

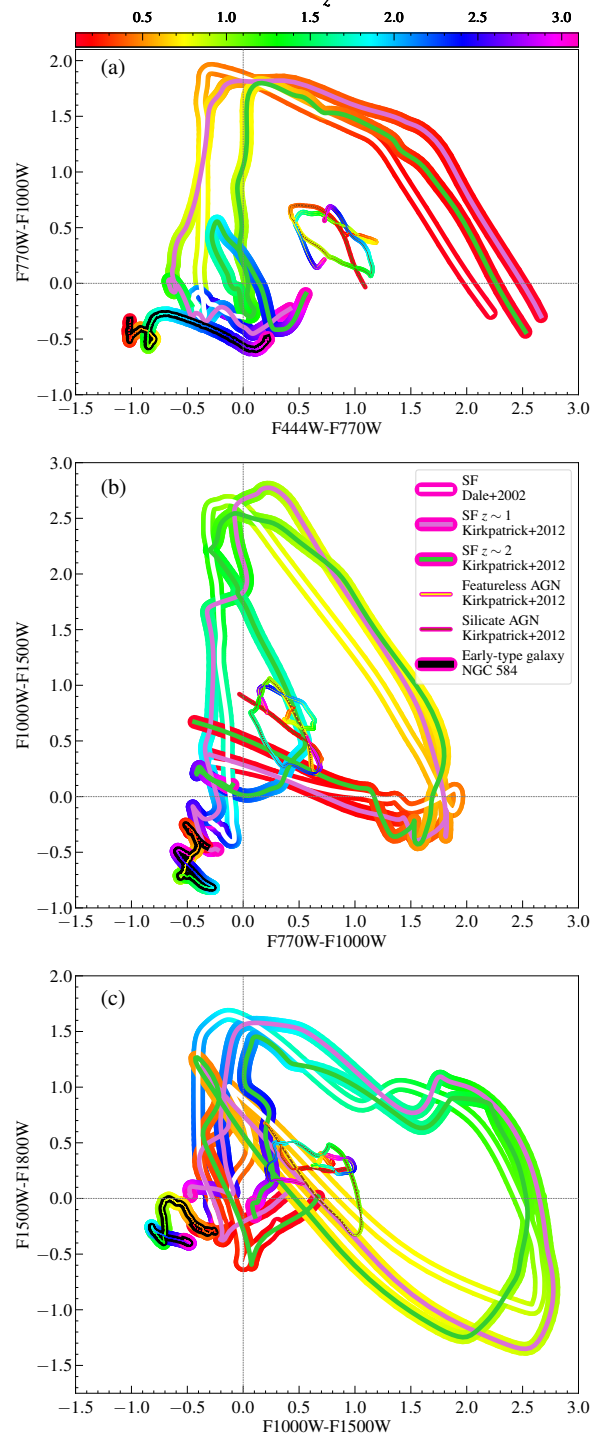


Figure 1. Redshift-dependent tracks of SFGs (thick lines), AGNs (thin lines), and quiescent galaxies (thick lines with thick-black filling) in mid-infrared color-color diagrams. From top to bottom: F444W–F770W vs. F770W–F1000W; F770W–F1000W vs. F1000W–F1500W; and F1000W–F1500W vs. F1500W–F1800W color-color diagrams based on SF SED templates from [Dale & Helou \(2002\)](#) and [Kirkpatrick et al. \(2012\)](#); AGN templates from [Kirkpatrick et al. \(2012\)](#); and the early-type SED of NGC 584.

observed spectra of normal SFGs spanning a wide range in far-infrared colors and dust temperature.

Kirkpatrick et al. (2012) created composite SED templates in the rest-frame 0.3–600 μm range for four sub-samples of 24 μm -selected $z \sim 0.5\text{--}4$ (U)LIRGs in the GOODS-N and ECDFS fields, classified based on a mid-infrared spectral decomposition. These sub-samples consist of $z \sim 1$ SF-dominated galaxies (SF $z \sim 1$, for short), $z \sim 2$ SF-dominated galaxies (SF $z \sim 2$), AGN-dominated galaxies with clear 9.7 μm silicate absorption (silicate AGN), and AGN-dominated galaxies with featureless mid-infrared spectra (featureless AGN). The SED template calibration sample consists of 95 galaxies with complete spectral coverage from IRAC, IRS, and MIPS on *Spitzer*, *Herschel* PACS and SPIRE, and ground-based 870 μm and 1.15 mm.

We calculate the *JWST* mid-infrared multi-band magnitudes for an SED template at a given redshift, using the SEDPY package (Johnson 2019; Johnson et al. 2021) to convert the redshifted spectra into response curve-determined mean flux in each band. Motivated by the SMACS J0723 observations (see Section 4), we generate F444W–F770W vs. F770W–F1000W; F770W–F1000W vs. F1000W–F1500W; and F1000W–F1500W vs. F1500W–F1800W color-color diagrams. These combinations are chosen such that each maximizes the color variations at a particular redshift range by including a relatively blue baseline PAH-unaffected filter as well as two redder filters tracing different PAH features. The F1800W filter allows tracing the strong 6.2 and 7.7 μm PAH features up to $z \sim 1.7$ and $z \sim 1.3$, respectively.

To generate the color-color diagrams we sample the redshift space from $z = 0.1$ to $z = 3.1$ in 0.01 intervals. At each sampled redshift, we calculate the colors for each of the SF-dominated SED templates in Kirkpatrick et al. (2012) as well as the SF template from Dale & Helou (2002) with $f_\nu(60\mu\text{m})/f_\nu(100\mu\text{m}) = -0.5232$. For each SF template, Figure 1 presents the color-color space tracks in the $z = 0.1\text{--}3.1$ range. In each diagram, the location of the SFGs depend strongly on their redshifts. At higher redshifts they settle in a stationary locus at the lower left of the diagrams, at slightly negative colors.

We also generate $z = 0.1\text{--}3.1$ tracks for AGNs and quiescent galaxies to compare with those of SFGs (Figure 1). AGNs are represented by the AGN-dominated SED templates of Kirkpatrick et al. (2012), while quiescent galaxies are represented by the SED of the early-type galaxy NGC 584 (Brown et al. 2014). AGNs populate a region in the diagrams that is generally distinct from SFGs and quiescent galaxies at all redshifts. Quiescent

galaxies populate the region toward the bottom-left of the stationary locus of the SF tracks. Their location are roughly independent of redshift because of their approximate power-law spectral energy distributions.

3. SIMULATED COLOR-COLOR DIAGRAMS

We next simulate realistic color-color diagrams of SFGs¹ by populating the redshift-dependent tracks taking into account the cosmic star-formation history, the SFR of individual galaxies, and the sensitivity of the *JWST* instruments. As described below, we first simulate the SFR distribution of individual galaxies from $z = 0.1$ to $z = 3.1$ over a given field of view (FOV). Then we convert the simulated redshift and SFR distribution into mid-infrared multi-band magnitudes, using the SF SED templates normalized according to the correlation between the SFR and PAH luminosity of SFGs.

Simulating the redshift and SFR distribution of individual galaxies requires knowledge of the total SFR at each redshift interval, as well as the distribution of star-formation over individual galaxies at that redshift. We sample the redshift space in 0.01 intervals, using the cosmic star-formation history relation of Madau & Dickinson (2014) to calculate the total SFR of the FOV at each redshift bin. In each bin, we then randomly distribute the total SFR over individual galaxies, using the interpolated SFRF(z) (star formation rate function) from Sobral et al. (2014) ($z < 2.23$) and Smit et al. (2012) ($z > 2.23$). While Madau & Dickinson (2014) and Smit et al. (2012) adopt a Salpeter IMF, Sobral et al. (2014) use a Chabrier IMF. We scale from the former to the latter by multiplying the SFRs by a factor of 1.59.

We convert the drawn redshift and SFR distribution into mid-infrared intrinsic luminosity of SFGs, adopting a linear correlation between the SFR and PAH luminosity (L_{PAH}) as calibrated in Xie & Ho (2019). Xie & Ho (2019) divided their sample based on stellar mass (M_\star) and showed that galaxies with $M_\star > 10^9 M_\odot$ are in general 100 times brighter in L_{PAH} than $M_\star < 10^9 M_\odot$ galaxies with the same SFR (see their Figure 3 and Table 3). To make this distinction, we estimate the stellar mass corresponding to the drawn SFRs, using the star-formation main sequence (MS) calibration from Speagle et al. (2014). For each drawn redshift and SFR, we randomly draw the stellar mass in a 1σ truncated 0.2 dex normal distribution centred on the mean stellar mass determined by the best-fit MS relation. The dispersion is

¹ AGNs are not included in these simulations because only a few AGNs are expected to be detected per MIRI FOV. See Section 5 for a more detailed discussion.

motivated by the true scatter of the MS relation. Since Speagle et al. (2014) adopt a Kroupa IMF, we multiply their stellar mass by 1.55 to convert from the Kroupa IMF to the Salpeter IMF. The resulting sample of drawn SFR, redshift, and stellar mass is then converted into PAH $7.7 \mu\text{m}$ luminosity, using the Xie & Ho (2019) conversion.

For each drawn SFR and redshift, we randomly select a SF SED template (see Section 2), re-scale the template to match the drawn intrinsic PAH $7.7 \mu\text{m}$ luminosity, and calculate the *JWST* mid-infrared magnitudes for the redshifted spectra following the method of Section 2. The top panels in Figures 2, 3, and 4 show the resulting color-color diagrams for a MIRI FOV, consisting only of SFGs with observed magnitudes below the limiting magnitudes of the *JWST* observations of the SMACS J0723 field (see Section 4). We expect 18, 15, and 11 SFGs per MIRI FOV to enter the diagrams in Figures 2, 3, and 4, respectively.

4. COLOR-COLOR DIAGRAMS FOR THE SMACS J0723.3–7327 FIELD

As a proof of concept, we analyze the NIRC*am* and MIRI Early Release Observations of the SMACS J0723 field (PID 2736, PI: Pontoppidan; Pontoppidan et al. 2022). The broad-band imaging consists of 6 overlapping NIRC*am* images in the F090W, F150W, F200W, F277W, F356W, and F444W filters reaching a point source sensitivity of $AB \sim 29.8$ mag, and 4 overlapping MIRI images in the F770W, F1000W, F1500W, and F1800W filters reaching 5σ depths of $AB \sim 26.3$, 25.1, 24.0, and 23.0 mag, respectively. For each filter, we acquire the photometry- and astrometry-calibrated data products from the Mikulski Archive for Space Telescopes (MAST), reduced using the 1.5.3 version of the *JWST* Calibration Pipeline². Here, we focus on the imaging in the mid-infrared bands F444W, F770W, F1000W, F1500W, and F1800W.

There is a significant astrometric offset (more than $1''$) between the NIRC*am* imaging and the MIRI imaging data products available on MAST. We correct this by re-aligning the image in each of the F356W³, F444W, F770W, F1000W, F1500W, and F1800W filters directly to *Gaia* stars, using the *Gaia* Starlink software. In the resulting re-calibrated images, the centroids of Source Extractor-identified (SE*xtractor*; Bertin & Arnouts 1996) point sources overlap within $0.1''$ across all the filters. We further calibrate the astrometry by cor-

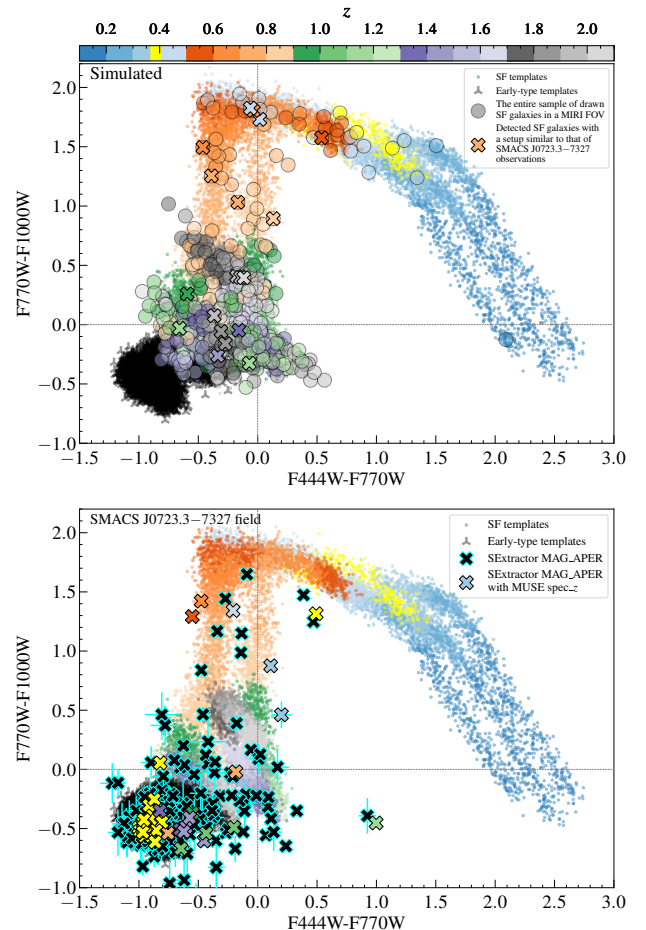


Figure 2. F444W–F770W vs. F770W–F1000W color-color diagram for the *JWST* observations of the SMACS J0723 field. Top panel: Simulated diagram for SFGs detected (filled crosses) in a MIRI FOV with the same magnitude limits as those of the SMACS J0723 observations. The open circles indicate the entire sample of SFGs in this FOV, most of which are undetected. The color-shaded tracks (small filled circles) are similar to the tracks of Figure 1, with an additional 0.05 mag scatter. The shaded black region shows the expected location of early-type galaxies. We expect to detect 18 SFGs per MIRI FOV. Bottom panel: Color-color diagram of 173 galaxies detected in *JWST* imaging (filled crosses), supplemented with MUSE spectroscopic redshifts where available (color-filled crosses). We identify 23 cluster galaxies with available spectroscopic redshifts ($z = 0.387 \pm 0.020$; yellow-filled crosses). There is only one confirmed cluster galaxy that resembles the color-color diagram location of SFGs (yellow-filled cross at (0.5,1.3); see Section 5).

recting the sky position of SE*xtractor*-detected stars ($CLASS_STAR > 0.5$) in F356W and F444W imaging against their position in MIRI imaging to achieve a sub-MIRI pixel offset between the point source centroids in the F356W/F444W and MIRI imaging. This astro-

² <https://jwst-pipeline.readthedocs.io>

³ The F356W imaging is only used to search for AGN candidates (see Section 5), and not in the production of color-color diagrams.

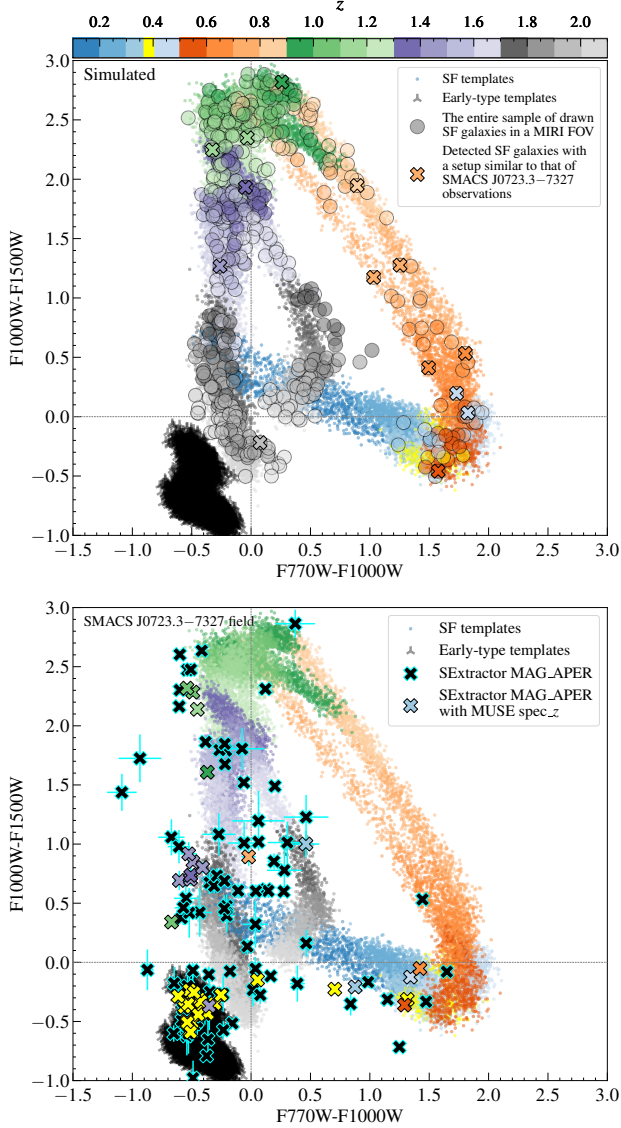


Figure 3. Same as Figure 2, but showing the $F770W-F1000W$ vs. $F1000W-F1500W$ colors for a total of 129 detections.

metric accuracy is sufficient for the purpose of cross-matching the detections in $F444W$ imaging with those in MIRI imaging.

We identify the bright sources in MIRI filters by running `SExtractor` in double-image mode. We use the imaging in $F770W$ as the detection image and adopt a `SExtractor` setup corresponding to a signal-to-noise ratio (SNR) of 2, setting `DETECT_MINAREA` = 4 and `DETECT_THRESH` = 1. This results in forced photometry of $F770W$ detections over the same sky segment across all MIRI filters. Similarly, we measure the photometry of bright $F356W$ and $F444W$ sources by running `SExtractor` in double-image mode with the

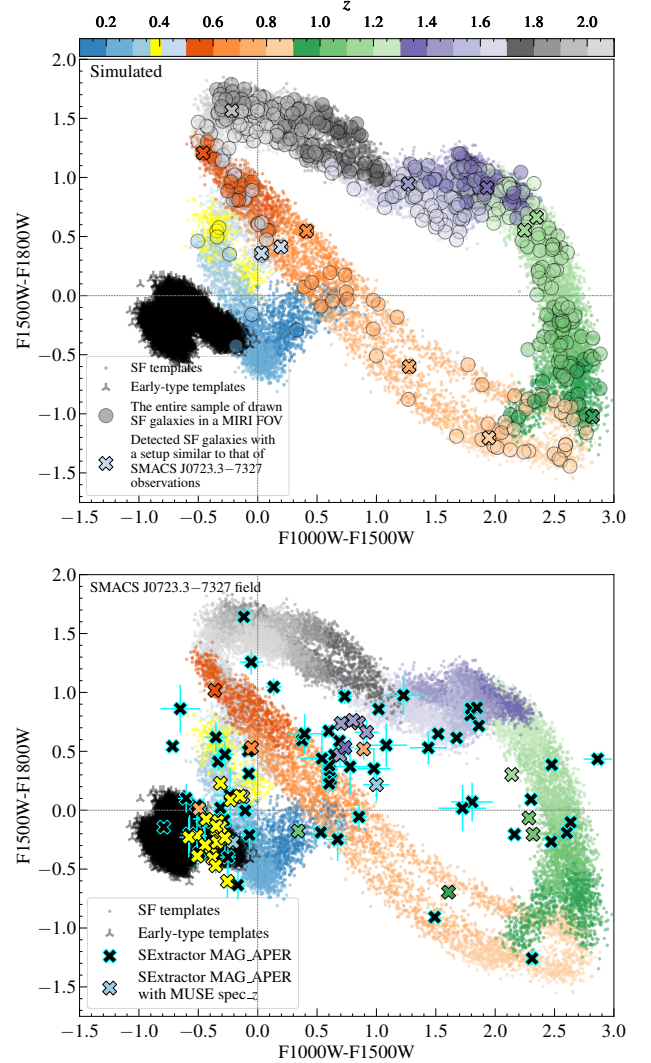


Figure 4. Same as Figures 2 and 3, but showing the $F1000W-F1500W$ vs. $F1500W-F1800W$ colors for a total of 99 detections.

$F444W$ filter as the detection image, `DETECT_MINAREA` = 4 and `DETECT_THRESH` = 1 (SNR = 2). We cross-match the NIRCcam and MIRI detections by matching the `SExtractor`-determined source centroid sky positions of the NIRCcam detections against MIRI detections within a $0.3''$ radius.

We use the `SExtractor`-measured aperture photometry (`MAG_APER`) within a $1''$ diameter as the measured magnitude in each filter. To check the robustness of colors measured in this way, we compare the `MAG_APER` colors with `SExtractor`-measured `MAG_AUTO` colors, which are measured by adopting a flexible aperture size determined for the source image in each filter by the second order moments of its light distribution. Generating the color-color diagrams with `MAG_AUTO` colors instead of

MAG_APER colors has no significant effect on the distribution of galaxies, and only slightly increases their scatter with respect to the simulated redshift-dependent tracks. The bias between the MAG_AUTO and MAG_APER colors is small (< 0.05 mag for all colors).

We use the most recent NIRCcam flux calibration (`JWST_0989.pmap`) to determine the zero-point magnitudes of F356W and F444W imaging. The photometry of MIRI imaging was calibrated using the default `JWST_0916.pmap` MIRI flux calibration used in the 1.5.3 version of the *JWST* calibration pipeline; this calibration is the same as the most recent calibration, `JWST_0989.pmap` . The mid-infrared color-color diagrams of the detected galaxies (filled crosses) are presented in the bottom panels of Figures 2, 3, and 4. In each diagram, we only plot the galaxies (`CLASS_STAR < 0.5`) where the estimated error of aperture photometry (`MAGERR_APER`) is below 0.2 mag (i.e., a $\sim 5\sigma$ detection) in all three bands.

Where available, we assign spectroscopic redshifts to the detected galaxies. The SMACS J0723 field was observed under the MUSE 0102.A-0718 program (Caminha et al. 2022), resulting in a spectroscopic redshift catalog containing 78 secure redshift measurements of *HST*-detected (Reionization Lensing Cluster Survey program, Coe et al. 2019) sources. We re-calibrate the astrometry of this catalog against our calibration of the NIRCcam and MIRI imaging by correcting the sky position of MUSE stars against that of F444W stars (F356W and F444W contain the highest number of star detections, resulting in 7 matches with the MUSE catalogue). We cross-match the MUSE catalog with the galaxies detected in F444W imaging, within a $0.3''$ radius. This results in assigning spectroscopic redshifts to 42, 41, and 36 galaxies in the diagrams of Figures 2, 3, and 4, respectively (color-filled crosses). Additionally, Carnall et al. (2022) measured 10 new spectroscopic redshifts for galaxies in the SMACS J0723 field based on the *JWST* NIRSpec medium-resolution data (PID: 2736). One of these galaxies at $z = 1.163$ (ID: 9483 in Carnall et al. 2022) enters the SMACS J0723 color-color diagrams (brown-filled cross).

5. DISCUSSION AND CONCLUSION

Overall, the detected galaxies occupy the regions of the color-color diagrams as predicted: SFGs in a specific redshift range stand out by several magnitudes from the bulk of detections occupying the region at the bottom left of the flat-spectrum (0,0) point, presumably populated by quiescent galaxies and higher redshift SFGs. Three non-cluster galaxies with available MUSE spec-

troscopic redshifts ($z = 0.42, 0.52, 0.60$; IDs⁴: 48, 49, 50) stand out by ~ 1.5 mag at the upper region of the F444W–F770W vs. F770W–F1000W color-color diagram (bottom panel of Figure 2). We confirm their classification as SFGs with spiral morphology through visual inspection. Two of these galaxies are marked with yellow circles in Figure 5.

For the cases where spectroscopic redshift is not available, the location of SFGs in the color-color diagrams can strongly constrain their redshifts. In Section 3 (see also Figure 1), we showed that the MIRI colors of SFGs can be highly sensitive to their redshifts. Therefore, photometric redshifts of SFGs can be estimated by comparing their location on the MIRI color-color diagrams with the synthetic redshift-dependent tracks. For instance, the white circles in Figure 5 show three SFGs with estimated redshifts of $z \sim 0.9$ – 1.3 . In Langeroodi et al. (2023, in prep.) we assess the accuracy of such mid-infrared derived photometric redshifts.

In Figure 2, we identify 23 galaxies associated with the cluster (yellow-filled crosses) based on MUSE spectroscopic redshifts ($z = 0.387 \pm 0.02$); this accounts for all the cluster galaxies identified in Caminha et al. (2022). In Figures 3 and 4, we identify 23 and 19 cluster galaxies, respectively. Almost all of the cluster galaxies (except for one; see below) occupy the region corresponding to quiescent galaxies, which is expected due to the higher efficiency of various quenching channels in cluster environments (see, e.g., von der Linden et al. 2010; Bahé et al. 2017; Donnari et al. 2021; Kim et al. 2022; Boselli et al. 2022). The light-blue circle in Figure 5 marks the brightest cluster galaxy (ID: 41). The excellent agreement between the color-color diagram region occupied by cluster early-type galaxies and their predicted location (see Section 2 and Figure 1), as is especially evident in Figures 3 and 4, verifies the accuracy of the adopted relative flux calibration for the MIRI filters (see Section 4).

We detect two galaxies located in front of the cluster (dark-orange crosses in each color-color diagram; ID: 21 and 22), which are consistent neither with the predicted colors of SFGs at their corresponding spectroscopic redshifts nor with early-type galaxies. We interpret these as SFGs with a significant contribution of quenched SED to their spectra. The linear combination of a quenched spectrum with that of a SFG results in moving the color-color diagram location of the galaxy toward the stationary locus of the quenched galaxies. Therefore, rather than being exclusively confined to the presented tracks,

⁴ Unless otherwise specified, throughout this work ID refers to ID in the spectroscopic redshift catalogue of Caminha et al. (2022).

some galaxies with significant quenched fraction end up populating the ‘forbidden’ region in-between.

The number counts of detected SFGs are in general agreement with our simulations. We expect fewer than one $z < 0.3$ and a handful of $0.3 < z < 0.5$ SFGs to enter the color-color diagrams, both of which are confirmed by the SMACS J0723 diagrams. However, we detect more galaxies than predicted at $z > 0.5$, where lensing starts to influence the number counts. We suspect that the excess detections are primarily caused by a combination of lensing magnification and multiple imaging (Mason et al. 2015). Two spectroscopically-confirmed multiply-imaged galaxies enter the diagram in Figure 2 including the $z = 1.4503$ 1.1, 1.2, and 1.3 images from Caminha et al. (2022) as well as the $z = 1.3782$ 2.1 and 2.3 images. The 1.1, 1.2, and 1.3 images also enter the diagrams in Figures 3 and 4. The 1.2 lensed image is marked with the green circle in Figure 5. Early-type galaxies with non-negligible star-formation can contaminate the $z > 0.5$ SFG number counts as well, especially in the F444W–F770W vs. F770W–F1000W diagram where the early-type region is close to the $z > 0.5$ SFG region.

We note that the method used herein for simulating the detected population of SFGs (see Section 3) relies on the SFR– L_{PAH} calibration of Xie & Ho (2019), which is derived from a sample of galaxies in the nearby Universe ($z < 0.3$). In particular, Xie & Ho (2019) suggested that at a fixed SFR, galaxies with $M_{\star} < 10^9 M_{\odot}$ are on average ~ 100 times fainter in L_{PAH} compared to galaxies with $M_{\star} > 10^9 M_{\odot}$; we assume that this is valid at redshifts beyond $z = 0.3$. This assumption strongly constrains the simulated number of SFG detections at $z > 0.5$, where at a fixed SFR the stellar mass of galaxies are on average at least 1.6 dex lower than at $z = 0$ (see Speagle et al. 2014). The extrapolation of this $10^9 M_{\odot}$ threshold to redshifts higher than $z = 0.3$ should be further investigated in field observations, where unlike the SMACS J0723 field the number counts are not boosted by lensing or dominated by quenched cluster galaxies.

Variations in the relative strengths of PAH emission features can potentially increase the observational scatter of SFGs with respect to the simulated redshift-dependent tracks in mid-infrared color-color diagrams. The relative strengths of PAH emission features are a function of the ionization state of grains and their size distribution (Draine & Li 2001; Maragkoudakis et al. 2020); this is especially pronounced for the $3.3\mu\text{m}$ and $11.3\mu\text{m}$ features. Since the $3.3\mu\text{m}$ feature at most contributes ~ 0.07 mag to the measured F444W or MIRI magnitudes (depending on the filter and redshift), variations in the relative strength of this feature do not catas-

trophically propagate into galaxy colors. In contrast, the $11.3\mu\text{m}$ feature can contribute as much as ~ 0.3 mag to the measured MIRI magnitudes; the pessimistic theoretically suggested 1 dex range for the relative strength of this feature (as shown in Maragkoudakis et al. 2020) can result in a ~ 0.2 mag scatter in mid-infrared colors. However, this entire range is not populated by observed SFGs.

Compared to the theoretically suggested range, observed SFGs in the nearby Universe ($z \sim 0$) exhibit a much smaller variation in the relative strengths of PAH emission features (Smith et al. 2007; O’Dowd et al. 2009; Wu et al. 2010; Stierwalt et al. 2014). For instance, in the Xie & Ho (2019) sample at $z < 0.3$ the line ratio of the $11.3\mu\text{m}$ to $7.7\mu\text{m}$ features varies by only ~ 0.1 dex (1σ distribution), which translates into a negligible 0.04 mag scatter in the observed MIRI colors of SFGs (smaller than the scatter implemented in the simulated tracks of Figures 2, 3, and 4). There is evidence that the scatter in the relative strengths of PAH features is larger at $z > 1$ compared to the nearby Universe (McKinney et al. 2020). McKinney et al. (2020) measured a 0.2 dex scatter in the line ratio of the $11.3\mu\text{m}$ to $6.2\mu\text{m}$ features at $z > 1$, which can translate into a 0.1 mag scatter in the measured MIRI colors. This might be affecting the location of SFGs in the color-color-diagrams of Figures 3 and 4, as is evident especially at $z > 1$ by the larger scatter with respect to the simulated tracks.

Lyu et al. (2022) predicted a few (~ 4) AGN detections per MIRI FOV. We detect one galaxy with strong point source emission in MIRI imaging ($\nu L_{\nu} \approx 4 \times 10^{42}$ erg s^{-1} at 10^{14} Hz). It has a spectroscopic redshift consistent with it being a cluster member ($z = 0.3822$; ID: 25; marked with the red circle in Figure 5). The location of this galaxy in the color-color diagrams is consistent with that of an SFG at its redshift. Therefore, from a color-color diagram point of view, this source could be an AGN in a star-forming galaxy. Such systems have recently been shown to resemble SFG PAH emissions (García-Bernete et al. 2022; Lai et al. 2022; Donnan et al. 2022), if the effect of AGN radiation fields on the excitation of PAHs in nuclear star-forming regions are not particularly strong (e.g. Lai et al. 2022). However, we do not find any X-ray detection associated with this source, and its F356W–F444W NIRCcam color (-0.21 mag ± 0.01) is not consistent with the W1–W2 > 0.8 AGN selection criterion (see, e.g., Stern et al. 2012). In the entire sample shown in Figure 2 and Table 5, we do not find any source with F356W–F444W > 0.8 .

This Letter has presented the first demonstration of *JWST* era color-selection of SFGs based on their PAH emission. Upcoming deeper/wider *JWST* mid-infrared

imaging will further populate the color-color diagrams presented herein, and allow the construction of large samples of normal SFGs (as well as quenched galaxies) at redshifts previously unexplored. Such samples can be instrumental in population studies of normal SFGs.

The authors would like to thank the anonymous referee who greatly helped in improving the presentation

and discussion. The authors would like to acknowledge initial discussions with Luis Colina and Hiroyuki Hirashita, as well as constructive comments from Sandra Raimundo. This work was supported by a VILLUM FONDEN Investigator grant (project number 16599). The *JWST* data used in this work were obtained from the Mikulski Archive for Space Telescopes (MAST) at the Space Telescope Science Institute. The specific NIR-Cam and MIRI observations analyzed can be accessed via [10.17909/v0ka-bd26](https://doi.org/10.17909/v0ka-bd26).

REFERENCES

- Bahé, Y. M., Barnes, D. J., Dalla Vecchia, C., et al. 2017, *MNRAS*, 470, 4186
- Bertin, E., & Arnouts, S. 1996, *A&AS*, 117, 393
- Boselli, A., Fossati, M., & Sun, M. 2022, *A&A Rv*, 30, 3
- Brown, M. J. I., Moustakas, J., Smith, J. D. T., et al. 2014, *ApJS*, 212, 18
- Caminha, G. B., Suyu, S. H., Mercurio, A., et al. 2022, arXiv e-prints, arXiv:2207.07567
- Carnall, A. C., Begley, R., McLeod, D. J., et al. 2022, arXiv e-prints, arXiv:2207.08778
- Coe, D., Salmon, B., Bradač, M., et al. 2019, *ApJ*, 884, 85
- Dale, D. A., & Helou, G. 2002, *ApJ*, 576, 159
- Donnan, F. R., García-Bernete, I., Rigopoulou, D., et al. 2022, arXiv e-prints, arXiv:2210.04647
- Donnari, M., Pillepich, A., Nelson, D., et al. 2021, *MNRAS*, 506, 4760
- Draine, B. T., & Li, A. 2001, *ApJ*, 551, 807
- . 2007, *ApJ*, 657, 810
- Förster Schreiber, N. M., Roussel, H., Sauvage, M., & Charmandaris, V. 2004, *A&A*, 419, 501
- García-Bernete, I., Rigopoulou, D., Alonso-Herrero, A., et al. 2022, arXiv e-prints, arXiv:2208.11620
- Inami, H., Armus, L., Matsuhara, H., et al. 2018, *A&A*, 617, A130
- Johnson, B. D. 2019, SEDPY: Modules for storing and operating on astronomical source spectral energy distribution, Astrophysics Source Code Library, record ascl:1905.026, , , ascl:1905.026
- Johnson, B. D., Leja, J., Conroy, C., & Speagle, J. S. 2021, *ApJS*, 254, 22
- Kim, K. J., Bayliss, M. B., Noble, A. G., et al. 2022, arXiv e-prints, arXiv:2207.12491
- Kirkpatrick, A., Pope, A., Sajina, A., et al. 2015, *ApJ*, 814, 9
- Kirkpatrick, A., Pope, A., Alexander, D. M., et al. 2012, *ApJ*, 759, 139
- Kirkpatrick, A., Alberts, S., Pope, A., et al. 2017, *ApJ*, 849, 111
- Lai, T. S. Y., Armus, L., U, V., et al. 2022, arXiv e-prints, arXiv:2209.06741
- Laurent, O., Mirabel, I. F., Charmandaris, V., et al. 2000, *A&A*, 359, 887
- Lyu, J., Alberts, S., Rieke, G. H., & Rujopakarn, W. 2022, arXiv e-prints, arXiv:2209.06219
- Madau, P., & Dickinson, M. 2014, *ARA&A*, 52, 415
- Maragkoudakis, A., Peeters, E., & Ricca, A. 2020, *MNRAS*, 494, 642
- Mason, C. A., Treu, T., Schmidt, K. B., et al. 2015, *ApJ*, 805, 79
- McKinney, J., Pope, A., Armus, L., et al. 2020, *ApJ*, 892, 119
- O’Dowd, M. J., Schiminovich, D., Johnson, B. D., et al. 2009, *ApJ*, 705, 885
- Pontoppidan, K., Blome, C., Braun, H., et al. 2022, arXiv e-prints, arXiv:2207.13067
- Pope, A., Chary, R.-R., Alexander, D. M., et al. 2008, *ApJ*, 675, 1171
- Sajina, A., Spoon, H., Yan, L., et al. 2009, *ApJ*, 703, 270
- Shiple, H. V., Papovich, C., Rieke, G. H., Brown, M. J. I., & Moustakas, J. 2016, *ApJ*, 818, 60
- Shiple, H. V., Papovich, C., Rieke, G. H., et al. 2013, *ApJ*, 769, 75
- Smit, R., Bouwens, R. J., Franx, M., et al. 2012, *ApJ*, 756, 14
- Smith, J. D. T., Draine, B. T., Dale, D. A., et al. 2007, *ApJ*, 656, 770
- Sobral, D., Best, P. N., Smail, I., et al. 2014, *MNRAS*, 437, 3516
- Speagle, J. S., Steinhardt, C. L., Capak, P. L., & Silverman, J. D. 2014, *ApJS*, 214, 15
- Stern, D., Assef, R. J., Benford, D. J., et al. 2012, *ApJ*, 753, 30
- Stierwalt, S., Armus, L., Charmandaris, V., et al. 2014, *ApJ*, 790, 124
- Treyer, M., Schiminovich, D., Johnson, B. D., et al. 2010, *ApJ*, 719, 1191

Veilleux, S., Rupke, D. S. N., Kim, D. C., et al. 2009, *ApJS*,
182, 628

von der Linden, A., Wild, V., Kauffmann, G., White, S.
D. M., & Weinmann, S. 2010, *MNRAS*, 404, 1231
Wu, Y., Helou, G., Armus, L., et al. 2010, *ApJ*, 723, 895
Xie, Y., & Ho, L. C. 2019, *ApJ*, 884, 136

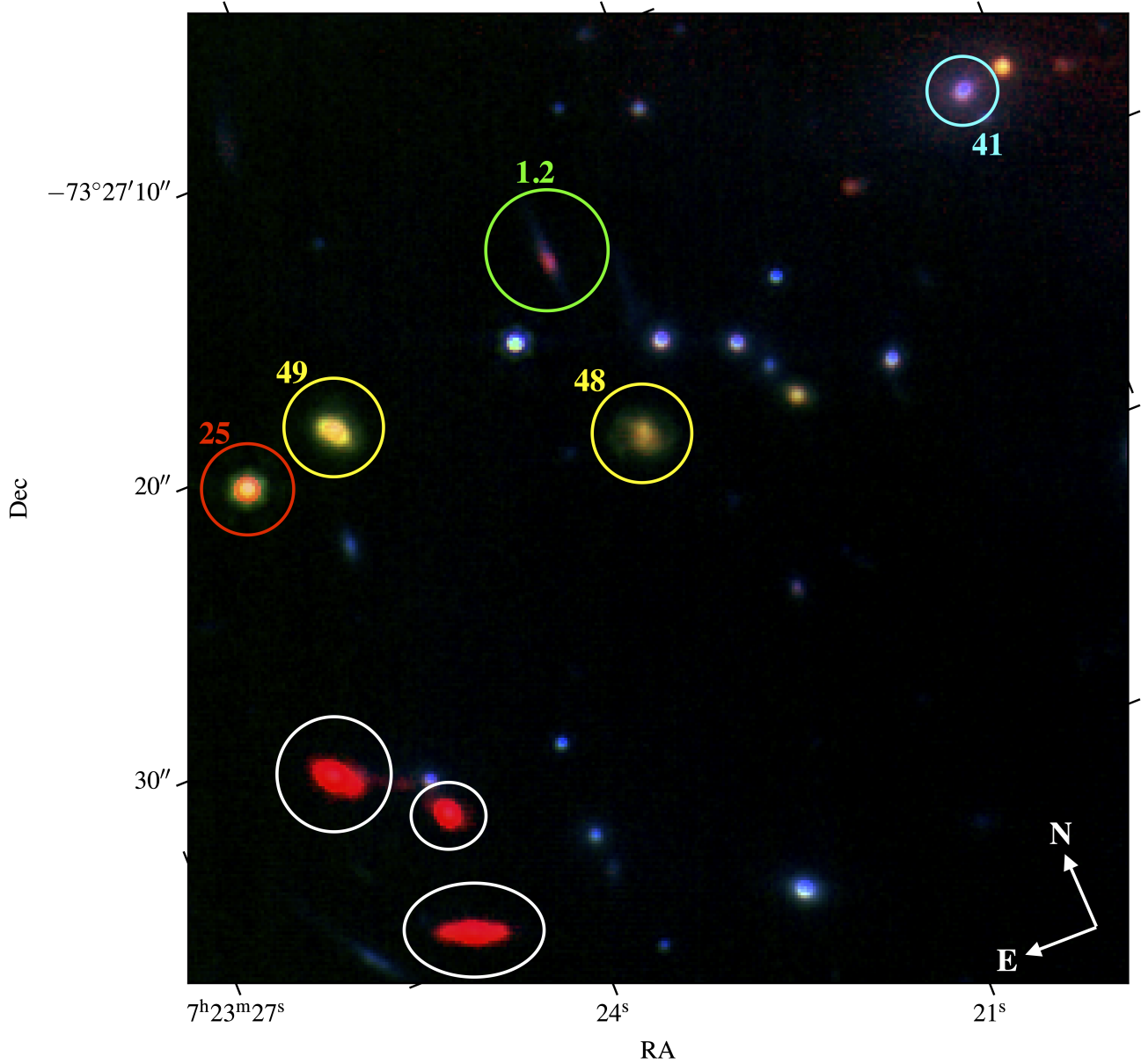


Figure 5. Color-composite image (F1500W: red, F1000W: green, F770W: blue) of a 320×310 pixel ($0.11''$ per pixel) except of the *JWST*/MIRI SMACS J0723 observations (see Pontoppidan et al. 2022, for the full FOV). The number next to each circle indicates the ID in the spectroscopic redshift catalog of Caminha et al. (2022). The yellow circles mark two SFGs at $z = 0.4233$ (ID: 48) and 0.5189 (ID: 49). The light-blue circle marks the brightest cluster (elliptical) galaxy (ID: 41). The green circle shows a lensed source at $z = 1.4503$ (ID: 1.2). We identify one cluster ($z = 0.3822$; ID: 25) SFG which is marked with the red circle. The white circles mark three SFGs at estimated $z \sim 0.9$ – 1.3 , as indicated by their location in the color-color diagrams.

ID	RA	DEC	F444W	F770W	F1000W	F1500W	F1800W	spec-z
130	110.8498258	-73.4625933	24.94 ± 0.01	24.74 ± 0.09	24.28 ± 0.07	23.28 ± 0.09	23.07 ± 0.11	0.3217
158	110.8488494	-73.4607803	22.71 ± 0.00	23.16 ± 0.02	23.77 ± 0.04	23.07 ± 0.07	22.60 ± 0.08	1.4792
159	110.8490125	-73.4603960	21.01 ± 0.00	21.92 ± 0.01	22.42 ± 0.01	22.76 ± 0.05	22.85 ± 0.09	0.397
163	110.8535771	-73.4596357	21.55 ± 0.00	21.75 ± 0.01	22.24 ± 0.01	19.96 ± 0.00	20.02 ± 0.01	1.0815
164	110.8537666	-73.4592641	20.97 ± 0.00	21.62 ± 0.00	22.29 ± 0.01	21.95 ± 0.02	22.12 ± 0.05	1.0823

Table 1. Measured photometry (in AB magnitudes) of the sources plotted in Figures 2, 3, and 4, as well as their MUSE or NIRSpc spectroscopic redshifts from [Caminha et al. \(2022\)](#) or [Carnall et al. \(2022\)](#), respectively. The photometry is measured in 1'' apertures (see Section 4). The full version of this table containing 172 objects, as well as the F356W photometry, and IDs in [Caminha et al. \(2022\)](#) or [Carnall et al. \(2022\)](#) catalogs (where available) is available online in machine-readable format.